MaNGA 8313-1901: Gas Accretion Observed in a Blue Compact Dwarf Galaxy?

Mengting Ju (居梦婷)[1,2], Jun Yin (尹君)[1,3], Rongrong Liu (刘蓉蓉)[1,2], Lei Hao (郝蕾)[1], Zhengyi Shao (邵正义)[1,3], Shuai Feng (冯帅)[4,5], Rogério Riffel[6,7], Chenxu Liu (刘辰旭)[8], David V. Stark[9,10], Shiyin Shen (沈世银)[1,3], Eduardo Telles[11], José G. Fernández-Trincado[12], Junfeng Wang (王俊峰)[13], Haiguang Xu (徐海光)[14], Dmitry Bizyaev[15,16], and Yu Rong (容昱)[17]

[1] Key Laboratory for Research in Galaxies and Cosmology, Shanghai Astronomical Observatory, Chinese Academy of Sciences, 80 Nandan Road, Shanghai 200030, People's Republic of China; jyin@shao.ac.cn
[2] University of Chinese Academy of Sciences, 19A Yuquan Road, Beijing 100049, People's Republic of China
[3] Key Lab for Astrophysics, Shanghai, 200034, People's Republic of China
[4] College of Physics, Hebei Normal University, 20 South Erhuan Road, Shijiazhuang 050024, People's Republic of China
[5] Hebei Key Laboratory of Photophysics Research and Application, Shijiazhuang 050024, People's Republic of China
[6] Departamento de Astronomia, Instituto de Física, Universidade Federal do Rio Grande do Sul, CP 15051, 91501-970, Porto Alegre, RS, Brazil
[7] Laboratório Interinstitucional de e-Astronomia—LIneA, Rua Gal. José Cristino 77, Rio de Janeiro, RJ—20921-400, Brazil
[8] Department of Astronomy, The University of Texas at Austin, 2515 Speedway Boulevard, Austin, TX 78712, USA
[9] Departments of Physics and Astronomy, Haverford College, 370 Lancaster Avenue, Haverford, PA 19041, USA
[10] Department of Astronomy, University of Washington, 3910 15th Avenue NE, Room C319, Seattle, WA 98195-0002, USA
[11] Observatório Nacional R. Gen. José Cristino, 77, 20921-400, Rio de Janeiro, Brazil
[12] Instituto de Astronomía, Universidad Católica del Norte, Av. Angamos 0610, Antofagasta, Chile
[13] Department of Astronomy, Physics Building, Xiamen University, Xiamen, Fujian, 361005, People's Republic of China
[14] School of Physics and Astronomy, Shanghai Jiao Tong University, 800 Dongchuan Road, Shanghai 200240, People's Republic of China
[15] Apache Point Observatory and New Mexico State University, P.O. Box 59, Sunspot, NM, 88349-0059, USA
[16] Sternberg Astronomical Institute, Moscow State University, Moscow, Russia
[17] Department of Astronomy, University of Science and Technology of China, No.96, JinZhai Road, Baohe District, Hefei, Anhui, 230026, People's Republic of China

Abstract

Gas accretion is an important process in the evolution of galaxies, but it has limited direct observational evidences. In this paper, we report the detection of a possible ongoing gas accretion event in a blue compact dwarf (BCD) galaxy, MaNGA 8313-1901, observed by the Mapping Nearby Galaxies and Apache Point Observatory (MaNGA) program. This galaxy has a distinct off-centered blue clump to the northeast (the NE clump) that shows low metallicity and enhanced star formation. The kinematics of the gas in the NE clump also seems to be detached from the host BCD galaxy. Together with the metallicity drop of the NE clump, it suggests that the NE clump likely has an external origin, such as gas accretion or galaxy interaction, rather than an internal origin, such as an H II complex in the disk. After removing the underlying host component, we find that the spectrum of the "pure" clump can match very well with a modeled spectrum containing a stellar population of the young stars ($\leqslant 7$ Myr) only. This may imply that the galaxy is experiencing an accretion of cold gas, instead of a merger event involving galaxies with significant preexisting old stars. We also find signs of another clump (the SW clump) at the southwest corner of the host galaxy, and the two clumps may share the same origin of gas accretion.

Key words: Dwarf galaxies – Star formation – Galaxy abundances – Galaxy kinematics

1. Introduction

Numerical simulations suggest that the accretion of the metal-poor gas from the cosmic web is a common process to fuel the formation of disk galaxies (Finlator & Davé 2008; Stewart et al. 2011; Altay et al. 2013). Gas accretion, often with lower metallicity compared to surroundings, might dominate the early growth of galaxies (Finlator & Davé 2008). Kennicutt (1998) showed there is a tight relation between the star formation rates (SFRs) and the total mass of gas, i.e., the Kennicutt-Schmidt law. However, the depletion time, defined as the gas mass divided by the SFR observed at the present day, is shorter than the cosmic time in many star-forming galaxies. This implies that there should be gas replenishment in their evolutionary history. For very nearby galaxies, such as the Milky Way, M31, and M33, the pristine gas accretion is also needed to explain the observed metallicity distribution function and the metallicity radial gradient (Yin et al. 2009; Kang et al. 2012).

The characteristics of the gas accretion seems to be related with the dark matter masses of the host halos in which the galaxies are located (Dekel et al. 2009). The most massive halos ($M_{\rm halo} > 10^{14} M_\odot$) are usually well virialized in the local universe. The radiation pressure competes with the gravity, making the cold gas hard to fall in. Gas accretion can happen more easily in less-massive halos, where the cold gas can directly feed the star formation of the galaxies (Fumagalli et al. 2011; Genel et al. 2012; Liu et al. 2019).

However, it is difficult to directly observe the accreting gas, as it is often diffused and extends to very large scales (~100 kpc), making the surface densities fall below the detection limit of most large surveys. There are many indirect observational evidences of gas accretion (Cresci et al. 2010; Sánchez Almeida et al. 2014). For example, the metallicity inhomogeneities, particularly the combination of phenomena of metallicity dropping and intense starbursts, as observed in

some blue compact dwarf (BCD) galaxies, could be one piece of evidence of cold-flow accretion (Crain et al. 2009; Sánchez Almeida et al. 2015; Mannucci et al. 2010; Lassen et al. 2021). There are simulations that can reproduce this phenomenon as well, in that the external gas accreted by host galaxies can lower the metallicity of star-forming gas and trigger the star formation simultaneously (Yates et al. 2012).

The strong star-forming activities triggered by the gas accretion can produce bright off-centered starburst clumps. This kind of off-centered starburst clumps is very abundant in high-redshift galaxies (Mannucci et al. 2010; Rauch et al. 2011; Elmegreen et al. 2013). As good analogs of these high-redshift star-forming galaxies (Papaderos & Östlin 2012), local dwarf galaxies also show various signs of star formation in their outskirts. Cignoni et al. (2019) discussed the tendency for dwarf irregulars to host young populations at large radii. Some nearby galaxies show extended UV disks, which means there may be star formation in their outer disks (Thilker et al. 2007). In addition, high velocity clouds are found in many nearby galaxies including our own Milky Way (Hernandez et al. 2013; Fraternali 2014), which may provide a source of material to be accreted to sustain the star formation in these galaxies. These local galaxies can give us suggestive clues to study the gas accretion event.

The large Integral Field Unit (IFU) surveys of nearby galaxies, such as the Mapping Nearby Galaxies and Apache Point Observatory survey (MaNGA; Bundy et al. 2015), provide various spatially resolved information that can be critical in studying possible gas accretion processes. For example, Hwang et al. (2019) analyzed the data from the MaNGA survey and found that some off-centered anomalously low-metallicity (ALM) regions, defined as having metallicity more than 0.14 dex lower than that implied by the stellar mass density and metallicity relationship ($\Sigma_* - Z$), may be produced by the impulsive accretion of gas. These ALM regions have higher specific SFRs and younger stellar populations, and they are more easily found in the blue low-mass galaxies than other galaxies. Employing a simple but intuitive inflow model, Pace et al. (2021) found that the metallicity profiles of the low-mass and noninteracting galaxies with ALM regions can be produced by large inflows. Some of the Hα blobs (Lin et al. 2017; Pan et al. 2020; Ji et al. 2021) may also be associated with gas accretion. The IFU observations can also provide spatially resolved kinematic information, which sometimes is crucial to identifying unique patterns induced by the gas inflows (Chen et al. 2016; Jin et al. 2016).

In this paper, we present a BCD galaxy, MaNGA 8313-1901, with a bright clump that may indicate a gas accretion scenario. The paper is organized as follows: In Section 2, we introduce the Dark Energy Spectroscopic Instrument (DESI) Legacy Imaging data and the MaNGA survey data of MaNGA 8313–1901. In Section 3, we analyze the structural and spectral properties of this galaxy. In Section 4, we discuss the possible gas accretion scenario for this galaxy. We summarize this paper in Section 5. Throughout this paper, we adopt the cosmological parameters of $H_0 = 70 \, \mathrm{km \, s^{-1} \, Mpc^{-1}}$, $\Omega_M = 0.3$, and $\Omega_\Lambda = 0.7$.

2. Data

In this work, we use the photometric data from the DESI Legacy Imaging Surveys (Dey et al. 2019) and the spatially resolved spectroscopic data from the MaNGA survey (Bundy et al. 2015). MaNGA 8313-1901 was imaged by the DESI

Legacy Imaging Surveys (Dey et al. 2019). The Legacy surveys provide images of three optical bands (g, r, and z) covering about 14,000 deg². They include three public projects: (1) the Beijing-Arizona Sky Survey (BASS; Zou et al. 2017) takes images at $32° \leqslant \mathrm{decl.} \leqslant 84°$ in the g and r bands; (2) the Mayall z-band Legacy Survey (Silva et al. 2016) provides the z-band images with the same region as BASS; and (3) the Dark Energy Camera Legacy Survey (Blum et al. 2016) targets the remaining ≈9350 deg² with the g, r, and z bands. In this paper, we only use the coadded g-band image from BASS (the Legacy Surveys DR8) to analyze the morphological structure of our target (Section 3.1). BASS uses the 90Prime camera (Williams et al. 2004) on the Bok 2.3 m telescope. The median 5σ detection limits of BASS are $g = 23.48$ and $r = 22.87$ AB mag, which are about 1 mag deeper than those of the Sloan Digital Sky Survey (SDSS) images.

The MaNGA survey has observed approximately 10,000 nearby galaxies within the redshift range of $0.01 < z < 0.05$ as part of the fourth generation of the SDSS-IV (Blanton et al. 2017). The survey uses 17 different hexagonal fiber-bundle IFUs ranging from 19 fibers, spanning a field of view (FOV) of 12″ in diameter to 127 fibers covering an FOV of 32″ in diameter (Drory et al. 2015). All fibers are fed into the Baryon Oscillation Spectroscopic Survey spectrographs (Smee et al. 2013) on the SDSS 2.5 m telescope at Apache Point Observatory (Gunn et al. 2006). The site seeing is ∼1″5, and the point-spread function (PSF) in a typical MaNGA reconstructed data cube can be characterized by a circular Gaussian distribution with an FWHM of 2″5 (Law et al. 2015; Yan et al. 2016a). The MaNGA spectrograph provides wavelength coverage from 3600 Å to 10300 Å with a spectral resolution of $R \sim 1100$–2200 (Law et al. 2016, 2021; Yan et al. 2016b). The MaNGA data used in this work is taken from the Data Analysis Pipeline (DAP) hybrid binning MPL-8 version (see Westfall et al. 2019 and Belfiore et al. 2019 for more details). The data cube has a spatial grid of 0″5 × 0″5.

MaNGA 8313-1901 is one of the BCDs in the MaNGA survey. It is the most noticeable galaxy in the BCD sample as having a large off-centered clump. MaNGA 8313-1901 is a low-redshift galaxy at $z = 0.02425$ with a stellar mass of $\log(M_*/M_\odot) = 8.88$ (the NASA-Sloan Atlas catalog, although the stellar mass is also estimated to be $\log(M_*/M_\odot) = 9.28$ by the Max Planck for Astrophysics (MPA)–Johns Hopkins University (JHU) catalog (Kauffmann et al. 2003a). The main properties of this galaxy are listed in Table 1. MaNGA 8313-1901 shows a high average surface brightness of $\mu_{g,r_{50}} = 19.89 \, \mathrm{mag/arcsec^2}$ within the half light radius r_{50} (Wake et al. 2017). In the Galaxy Zoo 2 classifications, this galaxy is unbarred (Willett et al. 2013).

In the top-left panel of Figure 1, we show the SDSS gri-band composite image. It covers $15″ \times 15″$, corresponding to $7.56 \, \mathrm{kpc} \times 7.56 \, \mathrm{kpc}$ at its redshift. The magenta hexagon indicates the coverage of the 19-fiber bundle of the MaNGA survey. The FWHM of PSF of this galaxy is 2″59 (1.31 kpc) in the g band. In this image, there is a giant clump that is located to the northeast direction of the host galaxy, which we name as the NE clump.

In the top-right panel of Figure 1, we show the spectra at the three spaxels in the galaxy, labeled as the red, black, and orange crosses in the top-left panel, respectively. The red cross is at the center of the NE clump, which will be more specifically defined in Section 3.1. The black cross is at the galaxy center. The orange cross is at the center of the other

Table 1
Properties of MaNGA 8313-1901

MaNGA 8313-1901 = SDSS J160108.90+415250.7	
Parameters	Data
MaNGA ID	1-248352
R.A. (J2000)	16:01:08.90
	(240°.28712)
Decl. (J2000)	+41:52:50.77
	(41°.88075)
z[a]	0.02425
d [Mpc]	103.932
M_{NUV} [mag][a]	−17.46
M_g [mag][a]	−18.64
M_r [mag][a]	−18.86
M_z [mag][a]	−19.03
$\log(M_*/M_\odot)$[a]	8.88
$\log(M_*/M_\odot)$[b]	9.28
$\log(M_{HI}/M_\odot)$[c]	9.37
$\log(M_{halo}/M_\odot)$[d]	11.03
Sersic index[e]	1.46 ± 0.04 (the host galaxy)
	0.19 ± 0.04 (the NE clump)
Effective radius[e] [kpc]	1.23 ± 0.13 (the host galaxy)
	0.29 ± 0.01 (the NE clump)

Notes.
[a] The NASA-Sloan Atlas catalog: http://www.nsatlas.org.
[b] The MPA–JHU catalog (Kauffmann et al. 2003a).
[c] Masters et al. (2019).
[d] Yang et al. (2007, 2012).
[e] See more details in Section 3.

clump, which will be defined in Section 3.2. The three spectra show strong emission lines. The emission lines of the NE clump at the center (the red spectrum) are significantly stronger than those of the center of the host galaxy (the black spectrum).

We select 376 spaxels (∼80%) with signal-to-noise ratios (S/Ns) of the Hα emission line higher than five from the MaNGA DAP data for further analysis. These spaxels all fall into the star formation region in the Baldwin-Phillips-Terlevich (BPT) diagram (Baldwin et al. 1981; Kewley et al. 2001; Kauffmann et al. 2003b). In the bottom-left panel of Figure 1, the flux map of the Hα emission line shows two strong peaks. The stronger Hα peak is located in the NE clump, while the other one overlaps well with the center of the host galaxy. The Hα flux is corrected for the dust attenuation using the Hα/Hβ ratio. The intrinsic line ratio is assumed to be 2.86, and the attenuation curve is adopted as in Calzetti et al. (2000). The spectra that we use to analyze the stellar population are corrected for the Milky Way extinction law (Fitzpatrick 1999). The bottom-right panel demonstrates the equivalent width (EW) map of the Hα emission line. The EW(Hα) in the NE clump is dramatically higher than that of all other spaxels of the galaxy.

3. The Physical Properties of MaNGA 8313-1901

3.1. The Optical Morphology

Both the SDSS image (the top-left panel of Figure 1) and the Legacy g-band image (the leftmost panel of Figure 2) show that the NE clump is probably structurally detached from the host galaxy. Therefore, we would like to separate the host galaxy and the NE clump morphologically.

We use the GALFIT v3.0.5 (Peng et al. 2002, 2010), a 2D fitting methodology software, to do the decomposition. According to the axis ratio and the position angle (PA) values listed in the NASA-Sloan Atlas catalog, we draw the major and minor axes with gray dashed lines in Figure 2. We define a fitting area shown as the black box, whose sides are parallel to the major and minor axes. The box is drawn to try to have little contamination from the NE clump, yet also to be as big as possible for characterizing the host. We fit the host galaxy within the black box by convolving a single Sérsic model with a PSF extracted from an unsaturated star with a high S/N (ID 391 in the eighth Data Release, DR8, of DESI) near MaNGA 8313-1901. When fitting the host galaxy, we fix the PA to be the value taken from the NASA-Sloan Atlas catalog. Changing the PA value a little bit will not affect the fitting results much. From left to right, Figure 2 exhibits the g-band image taken from the DESI Legacy Imageing Survey, the best-fit 2D model of the host galaxy, the host-subtracted residual image, and the 1D surface brightness profile. The color scale is the same for all three images, and ranges from −0.25–20 nanomaggies[18] arcsec^{-2}. The NE clump is clearly shown in the residual image. The best-fit Sérsic index and the effective radius of the host component are $n = 1.46 \pm 0.04$ and $r_e = 1.23 \pm 0.13$ kpc, respectively ($2''.44 \pm 0''.26$). These two parameters are comparable to typical values of BCDs in general (Amorín et al. 2009).

We also use GALFIT to analyze the structure of the NE clump using the residual image after subtracting the best-fit host galaxy, as shown in the right panel of Figure 2. We use a single Sérsic model and the same PSF model extracted from ID 391 to fit the image in the gray box (∼3″ × 6″) defined to include mostly the NE clump. The best-fit Sérsic index and the effective radius of the fitted NE clump are $n = 0.19 \pm 0.04$ and $r_e = 290 \pm 12$ pc ($0''.57 \pm 0''.24$). The radial profiles of the host galaxy (black dots) and the NE clump (red dots) are shown in the rightmost panel of Figure 2. In this panel, we also show the PSF profile with yellow dots. We can see that the NE clump is more extended than the PSF. Therefore, the size we measured for the NE clump is real. The diameter of the NE clump is 580 pc, which is significantly larger than those of local clumps, and is comparable to the typical sizes (∼1 kpc) of the clumps at high redshifts (Lagos et al. 2007; Elmegreen et al. 2013; Wuyts et al. 2014; Meng & Gnedin 2020).

We draw a red circle with a radius of $1''.71$ (three times the effective radius of the NE clump) in Figure 2, centered at the center of the NE clump obtained from the GALFIT fitting. We define this region as the NE clump region of our BCD galaxy.

3.2. Star Formation and Gas-phase Metallicity

With the MaNGA data, we can measure the SFR and the gas-phase metallicity of each spaxel in the data cube, then obtain the map of the SFR and the metallicity for the whole galaxy. Since all of the analyzed spaxels are located in the star formation branch in the BPT diagram (Baldwin et al. 1981; Kewley et al. 2001; Kauffmann et al. 2003b), we use the dust-corrected Hα luminosity to calibrate the SFR with Equation (1), taken from Kennicutt & Evans (2012) and

---

[18] The definition of the unit "nanomaggy" can be found here: https://www.sdss.org/dr17/algorithms/magnitudes/.

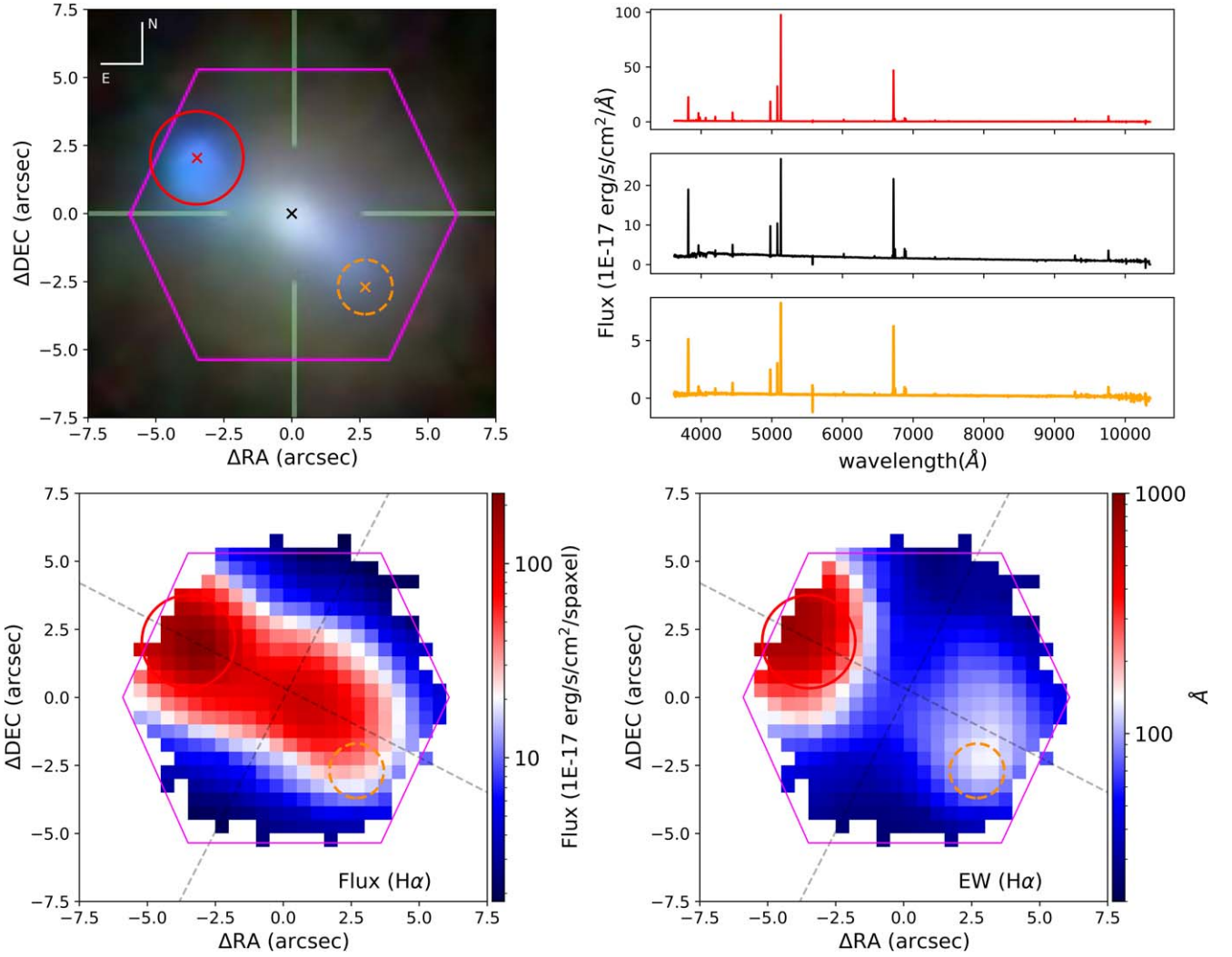**Figure 1.** The top-left panel shows the SDSS *gri* composite image, which covers $15'' \times 15''$ in size and corresponds to 7.56 kpc $\times$ 7.56 kpc at its distance. The magenta hexagon shows the coverage of the MaNGA bundle in this field. The red solid circle and the orange dashed circle are the locations of the NE clump and the SW clump, defined in Sections 3.1 and 3.2, respectively. In the top-right panel, the spectra of three spaxels indicated as red, black, and orange crosses in the top-left panel are shown as the red, black, and orange solid lines, respectively. Bottom left: the dust-corrected flux map of the Hα emission line. Bottom right: the equivalent width (EW) map of the Hα emission line. The major and minor axes are shown as dashed gray lines. The position angle is adopted from the NASA-Sloan Atlas catalog.

Hao et al. (2011).

$$\log\left(\frac{\mathrm{SFR}}{M_\odot\,\mathrm{yr}^{-1}}\right) = \log\left(\frac{L_{\mathrm{H}\alpha}}{\mathrm{erg\,s^{-1}}}\right) - 41.27 \qquad (1)$$

The SFR map is shown in the left panel of Figure 3. This map shows an enhanced star formation in the NE clump, and the value of the SFR in these spaxels is almost twice the SFRs in the spaxels at the galaxy center. The total SFR of the NE clump region (within the red circle) and that of the rest area, by summing up the SFRs in corresponding spaxels, are $0.417 \pm 0.013\,M_\odot\,\mathrm{yr}^{-1}$ and $0.829 \pm 0.017\,M_\odot\,\mathrm{yr}^{-1}$, respectively.

We use the MaNGA data cube and the MEGACUBE software to obtain the spatially resolved stellar populations (Mallmann et al. 2018; Riffel et al. 2021) of our galaxy. MEGACUBE is based on the STARLIGHT code (Cid Fernandes et al. 2005), but can be applied to a cube data. The stellar mass and age of each spaxel can be obtained by this code. The mass of the NE clump and that of the rest area are $3.33 \times 10^8\,M_\odot$ and $3.72 \times 10^9\,M_\odot$, respectively. So the specific SFR of the NE

clump region and that of the rest area are $1.24 \times 10^{-9}\,\mathrm{yr}^{-1}$ and $2.23 \times 10^{-10}\,\mathrm{yr}^{-1}$.

The significantly enhanced star formation activity in the NE clump suggests that this region contains massive star clusters that have been recently formed. The integrated flux of Hβ is log $L(\mathrm{H}\beta) = 40.32$ [erg s^{-1}], which is large. Given its high luminosity and large size, the NE clump is likely to be an ensemble of unresolved massive star clusters (Lagos et al. 2011; Telles & Melnick 2018), rather than one massive cluster, even though it is hard to tell with the current available images of limited spatial resolutions.

In Figure 4, we show the light-weighted age map (the left panel) and the mass-weighted age map (the right panel) also obtained from the MEGACUBE software. The young stellar population contributes a significantly higher fraction to the light than to the mass. Therefore, the light-weighted stellar age will be severely younger than the mass-weighted age if the young stars dominate the stellar population. This is clearly shown as the difference between these two age maps in the NE
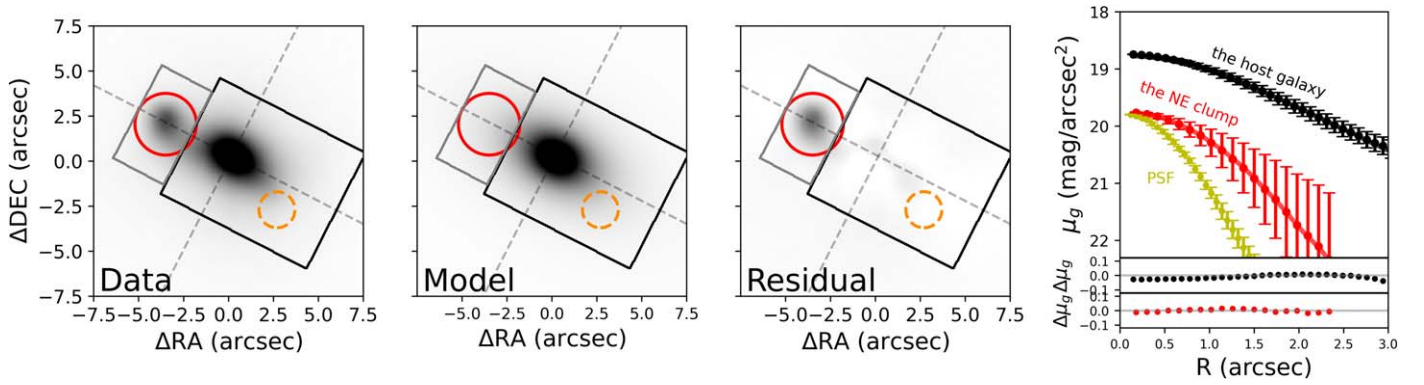
Figure 2. Two-dimensional surface brightness modeling of the host galaxy of MaNGA 8313-1901 with `GALFIT`. The leftmost panel shows the observed g-band image of BASS with a pixel size of $0\rlap{.}''06$ and a PSF FWHM of $1\rlap{.}''68$. The black box is defined to be the fitting area of the host galaxy. The gray box with a size of $\sim 3'' \times 6''$ and centered at the peak of Hα flux in the NE clump is the region we fit to obtain the morphological parameters of the NE clump with a size of $\sim 3'' \times 6''$. The best-fitted 2D model of the host galaxy given by `GALFIT` and the host-subtracted residual image are shown in the second and third panels. The color scale is the same for all images, and ranges from -0.25–20 nanomaggies arcsecond^{-2}. The two gray dashed lines show the major (northeast–southwest direction) and the minor (northwest–southeast direction) axes. In the left three panels, the red solid circle indicates our definition of the NE clump region with a radius of $1\rlap{.}''71$. The orange dashed circle with a radius of $1''$ shows our definition of the SW clump (Section 3.2). The rightmost panel shows the surface brightness profiles of the host galaxy (black), the NE clump (red), and the scaled PSF model (yellow). The dots with error bars demonstrate the observed data, and the lines stand for the 1D profiles of the best-fit `GALFIT` model. The two bottom subpanels of the rightmost panel are the residual ($\mu_{\rm data} - \mu_{\rm model}$) profiles of the surface brightness of the host galaxy (black) and the NE clump (red), respectively.

clump region in Figure 4, indicating that in the NE clump, the young stellar population dominates.

There are various methods to measure the gas-phase metallicity from the spectrum, such as the direct method and the strong-line methods. The direct method is sometimes referred to as the electron temperature (T_e) method. T_e can be estimated by the strength ratio of an auroral line to a line of lower excitation level of the same element. Usually, O III $\lambda 4363/\lambda 5007$ is used to estimate the T_e in the classical H II region model. Unfortunately, O III $\lambda 4363$ is often too weak to be measurable in normal galaxies.

To overcome this issue, people developed empirical methods, which use various strong emission lines that can be observed in the optical. The popular strong-line methods include the R23 method, where R23 $= \log \frac{[\text{O II}]\lambda\lambda 3727,9 + [\text{O III}]\lambda\lambda 4959,5007}{H\beta}$ (Pagel et al. 1979; Tremonti et al. 2004; Henry et al. 2013), the O3N2 method, where O3N2 $= \log \frac{[\text{O III}]\lambda 5007 / H\beta}{[\text{N II}]\lambda 6584 / H\alpha}$ (Pettini & Pagel 2004; Marino et al. 2013), and the N2 method, where N2 $= \log \frac{[\text{N II}]\lambda 6584}{H\alpha}$ (Storchi-Bergmann et al. 1994; Denicoló et al. 2002; Marino et al. 2013). Marino et al. (2013) calibrated the O3N2 method with observations of H II regions based on the direct T_e method:

$$12 + \log(\text{O/H}) = 8.533[\pm 0.012] - 0.214[\pm 0.012] \times \text{O3N2}. \tag{2}$$

This new calibration has been used to measure the metallicity of star-forming galaxies in several works (e.g., Lima-Costa et al. 2020; Ji et al. 2021). In our work, we also use this calibration to measure the metallicity of MaNGA 8313-1901.

In the middle and right panels of Figure 3, we show the gas-phase metallicity map derived from Equation (2), and its associated map of errors. A significant drop can be seen in the NE clump region. We further find another region to the southwest direction of the galaxy also with slightly lower metallicity compared to the host, although the drop of metallicity compared to the host center is within the error bars. We name this region the southwest (SW) clump, marked by an orange dashed circle with a radius of $1''$ in Figure 3. We

also label this same circle in the previous figures. The SW clump will be discussed in more detail in Section 4.

We show the metallicity of every star-forming spaxel of MaNGA 8313-1901 as a function of galactocentric distance in the left panel of Figure 5. There is a prominent population of spaxels with low metallicity. In order to check if these low-metallicity spaxels are all associated with the NE clump, we present the metallicity distribution as a function of the distance to the spaxel with the highest Hα flux in the NE clump ($r_{\rm NE}$) in the middle panel of Figure 5. The spaxels in the NE clump (within the red circle in the rightmost panel of Figure 5) and those in the SW clump (within the orange dashed circle in the rightmost panel of Figure 5) are colored with red and orange.

In the middle panel of Figure 5, we find that there are two distinct populations that can be well separated by the green dashed line. The spaxels with metallicity below the green dashed line are all spatially located in the region northeast of the black line in the g-band image integrated from the MaNGA data cube (the right panel of Figure 5); the spaxels with metallicity above the green dashed line are located in the remaining area. The low-metallicity region, as is shown by the region northeast of the black solid line, and the NE clump is spatially well correlated. We also notice that the region located northeast of the black line is larger than the morphologically defined NE clump region (the red circle in Figures 2 and 5). This is probably because the gas of the low-metallicity population is more extended than what can be identified by morphology.

We mentioned earlier in this section that there are multiple methods to estimate the metallicity besides the O3N2 method. We check whether our main conclusions about the metallicity based on the O3N2 method still stand with the R23 method and the direct method. In the left panel of Figure 6, we show the metallicity map obtained using the R23 method (Tremonti et al. 2004). We can see that this metallicity map has a similar feature to that obtained by the O3N2 method in the right panel of Figure 3. The metallicity of the NE clump is overall lower than that of the host galaxy.

In the MaNGA data cube, the [O III]$\lambda 4363$ auroral line can be observed in some spaxels. This makes the direct method
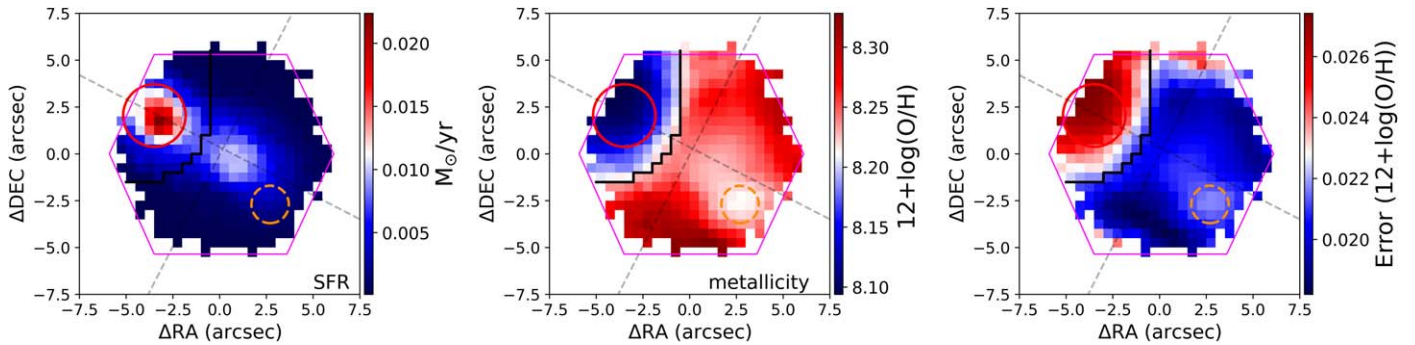
Figure 3. The SFR map (the left panel) and the metallicity map (the middle panel) with the metallicities measured via the O3N2 method. The error map of the metallicity measurements is shown in the right panel. The red circle indicates the NE clump region, and the orange dashed circle shows the SW clump region.
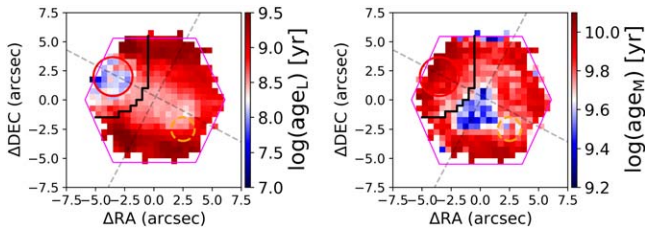

Figure 4. The maps of the light-weighted stellar age (the left panel) and the mass-weighted stellar age (the right panel).

possible. From the MaNGA pipe3D (Sánchez et al. 2016a, 2016b), we select spaxels with S/Ns of [O III]λ4363 larger than five, and then visually check to see whether the [O III]λ4363 is indeed real. In the end, there are 61 spaxels selected to have the [O III]λ4363 detected. We calculate the metallicities of these 61 spaxels using the bayesisan model-based code HII-CHI-mistry v5.1 (Pérez-Montero 2014), which uses the direct T_e method. The spatial location and metallicity of the 61 spaxels are shown in the middle panel of Figure 6. These spaxels are all in the low-metallicity region defined in Figure 5, and show low metallicities. In the right panel of Figure 6, we compare the metallicity derived by the O3N2 method to that derived from the direct method. The metallicity given by the direct method is systematically lower (∼0.1 dex) than that given by the O3N2 method. Overall, Figure 6 shows that the metallicity of the NE clump is consistently lower than that of the host galaxy with the various metallicity-measurement methods we checked.

3.3. Kinematics

In the left panel of Figure 7, we show the Hα velocity map taken from the MaNGA DAP data cube. The velocity field of the host galaxy is dominated by a rotating disk whose minor axis falls along the SE–NW direction. The NE clump lies close to the SW–NE major axis of the rotating disk of the host. The NE clump seems to be kinematically detached from the rotating disk of the host galaxy. In the middle panel of Figure 7, we model the velocity field of the Hα emission line of the host galaxy. The adopted rotation curve (Andersen & Bershady 2013) is as follows:

$$V(R) = v_{rot} \tanh(R/r_{rot}),   (3)$$

where r_{rot} is the turn-over radius, within which the rotation velocity increases with the radius R until it reaches the maximum velocity v_{rot} at r_{rot}. With Equation (3), the 2D

velocity field can then be obtained as

$$V_{obs}(R, i) = V_{sys} + V(R) \cdot \sin i \cdot \cos \phi,   (4)$$

where V_{sys} is the systematic recession velocity, $V(R)$ is the intrinsic rotation curve as defined by Equation (3), i is the inclination angle of the rotating disk, and ϕ is the azimuthal angle in the galaxy plane. We use emcee (Foreman-Mackey et al. 2013) to perform the velocity field fitting. In order to remove the contamination from the NE clump, we exclude in the fitting the metallicity defined NE clump region, i.e., the spaxels northeast of the black solid line (defined in Figure 5).

The best-fit velocity map is displayed in the middle panel of Figure 7, and the residual map is shown in the right panel. The parameters of the best-fit model are $i = 75°.3 \pm 14°.4$, $\phi = -161°.5 \pm 9°.8$, $v_{rot} = 90.7 \pm 32.5$ (km s^{-1}), and $r_{rot} = 6''.9 \pm 1''.6$. The errors represent the 67% confidence interval. From the residual map, we find that the NE clump has a systematic velocity toward us relative to the host galaxy, implying that this clump is a kinematically independent component. In this map, disturbance around the SW clump in the southwest corner is also weakly present.

Usually, bars in galaxies can also induce disturbances in the gas kinematics. However, the line-of-sight residual velocity of the gas at the NE clump region is quite significant at ∼25km s^{-1}, almost comparable to the maximum rotation velocity of the gas in the MaNGA field. In addition, the maximum residual velocity tends to be distributed toward the edge of the galaxy, instead of around the center. Thus, we think the velocity disturbances of the gas at the NE clump are unlikely to be induced by a bar in the galaxy, which is weak at most, if it exists at all judging from its morphology.

4. Discussion

An enhanced star formation complex in a galaxy can be induced by galaxy interactions or an infall of gas accretion, or by secular processes, such as a bar. It can also be merely a giant star-bursting complex produced internally in the disk. Indeed, a similar case (Richards et al. 2014) was reported in the Sydney-Australian-Astronomical-Observatory Multi-object Integral-Field Spectrograph (Croom et al. 2012; Allen et al. 2015) survey. There is an off-centered luminous clump in a dwarf galaxy, GAMA J141103.98-003242.3, and the clump also shows lower metallicity and higher SFR compared to the host galaxy. However, in this galaxy, they found no obvious distortion in the kinematic map of the Hα emission line; thus, they proposed that this clump may just be an intrinsic
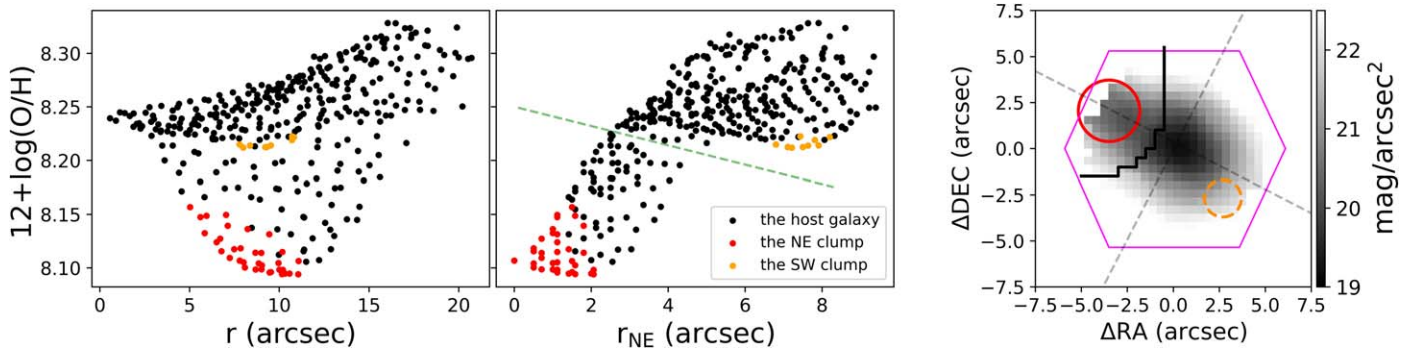
Figure 5. Left: the radial distribution of metallicity for every MaNGA spaxel. Middle: the offset metallicity radial distribution. The radius is defined as the distance to the spaxel with the highest Hα flux in the NE clump. There are two branches in this panel, well separated by the green dashed line. Right: the g-band image from the MaNGA survey. The red circle is the NE clump region, and the orange dashed circle shows the SW clump region. The black line is a dividing line of spaxels located between the two branches shown in the middle panel. The red, orange, and black data points in the left panel and the middle panel represent the spaxels in the NE clump, the spaxels in the SW clump, and all other remaining spaxels in the right panel, respectively.

stochasticity of star formation in a stable system of the host. This is different from MaNGA 8313-1901. In Figure 7, we show the Hα velocity map and the residual velocity map after subtracting a rotating disk. The kinematics of the ionized gas in the NE clump suggests that it is detached from the host. This and the significant drop of the metallicity in the NE clump together point more toward the NE clump being triggered by an external cause, such as galaxy interactions or gas accretion processes, rather than an internal star-bursting event. The much larger size of the NE clump compared to local star-bursting complexes also hints its external origin.

Therefore, for the remainder of the paper, we focus our discussions on the external origin of the NE clump. We explore further the type of external origin the NE clump can have, mainly distinguishing between the gas accretion process and that induced by the interactions. Cold streams of pristine gas may directly flow into the disk and even to the central regions of a galaxy, particularly in a less-massive halo (Joung et al. 2012; Peng & Maiolino 2014). According to the Wang et al. (2016, 2018) catalog, MaNGA 8313-1901 seems to be in a large-scale filamentary structure, where the cold gas reservoir can be more abundant than in clusters. Its host halo mass is estimated to be $M_{halo} = 10^{11.03} M_\odot$ (Yang et al. 2007, 2012). In such a halo, the cold gas is more likely to fall into the galaxies compared to galaxies in massive halos (Dekel et al. 2009). Thus, the environment of MaNGA 8313-1901 can accommodate both external scenarios.

In the gas accretion scenario, the accreted gas can come from the circumgalactic medium, the intergalactic medium, and/or even a companion galaxy, such as a gas-rich satellite (Hwang et al. 2019). The NE clump should contain only young stars that were just formed by the current star formation induced by the newly accreted gas. If the NE clump is induced by the galaxy–galaxy interactions instead, we would expect to see the old stellar populations from both the interacting galaxies. Thus, we explore the origin of the NE clump mainly by checking whether there are any significant old stellar populations associated with it.

The observed spectrum in the NE clump region, which we obtain by summing up the observed spectra of all spaxels in the red circle, and shown in light blue in Figure 8, includes light from both the NE clump and the underlying host galaxy in the same region. Therefore, to evaluate the stellar population of the NE clump itself, we need to subtract the spectrum of the underlying host galaxy component in the NE region. This can

be done by constructing a spectrum of the host galaxy component, by assuming a proper spectral shape, and then scaling it to the flux of the host galaxy component in the red circle.

We use the image decomposition results obtained in Section 3.1 to estimate the g-band flux of the underlying host component in the NE clump region in MaNGA 8313-1901. The structural parameters of the host galaxy obtained from the morphology decomposition (Figure 2) are used to construct a full-scale (including the NE clump region) image of the pure host, which is then convolved with the PSF to produce what would be the observed g-band image of the pure host galaxy in MaNGA 8313-1901. The total g-band flux of the underlying host component within the NE clump region (the red circle in Figure 2) can then be estimated from the constructed host image to be $flux_{host\_in\_clump} = 10.83 \times 10^{-17}$ erg s^{-1} cm^{-2}.

Next, we assume the spectral shape of the underlying host galaxy component in the NE region is the same as that at the galaxy center. This assumption is reasonable because the low-mass galaxies often show flat slopes in their mass-to-light ratio (M/L) gradients, which suggests that the stellar population of the host galaxy is similar from the inside out (Ge et al. 2021). We obtain a spectrum by summing up the spectra of all spaxels within an aperture of a diameter of $2\rlap{.}{''}5$ around the galaxy center, and adopt its shape for the underlying host galaxy component. Together with the g-band flux of the underlying host component estimated above, we can then construct the spectrum of the underlying host component in the NE clump region. This is shown as the light orange spectrum in Figure 8.

Then we subtract the constructed underlying host-component spectrum (the light orange spectrum in Figure 8) from the observed spectrum (the light blue spectrum in Figure 8) to obtain the "pure" clump spectrum (called so hereafter), which is shown as the black line in Figure 8. The strong continuum in the blue wavelengths and the weak Balmer break suggest that the stellar populations of the "pure" NE clump are young (Guseva et al. 2007).

In addition, the "pure" clump spectrum is almost free of absorption lines. In Figure 9, we zoom in on the observed NE clump spectrum (the blue line), the spectrum of the underlying host component in the NE clump region (the orange line), and the "pure" clump spectrum (the black line) for some of the absorption lines often used to indicate stellar populations. Absorption lines, such as Hβ, Hδ, Ca II λ3933, 3968, and Ca II λ8500, 8544, are clearly seen in the observed spectrum (blue)
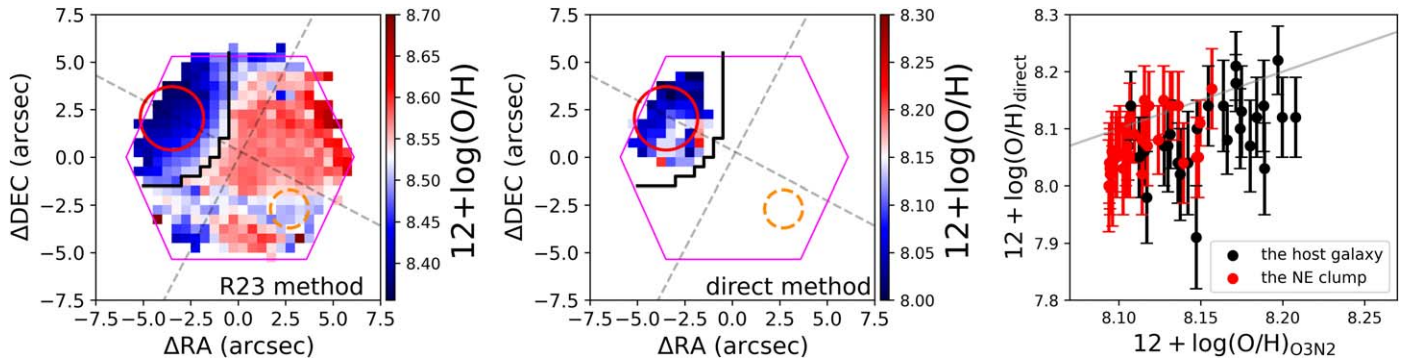
Figure 6. Left: the metallicity map obtained via the R23 method. Middle: the metallicity map obtained via the direct T_e method. Only 61 spaxels with significant O III $\lambda4363$ detections (S/N > 5) are shown. Right: the comparison between the metallicities obtained from the direct method and those obtained from the O3N2 method for the 61 spaxels in the middle panel. The red data points and the black data points represent the spaxels inside and outside the morphologically defined NE clump (the red circle in the middle panel), respectively. The gray line is the one-to-one correlation.

and the underlying host spectrum (orange), but in the "pure" clump spectrum (black), they all become very insignificant. In particular, a series of higher-ordered Balmer and He absorption lines that appear in the first panel of Figure 9 are all very well subtracted. Note that our orange spectrum is not a fit to the observed spectrum. It is constructed using just the spectral shape of the host galaxy and the flux obtained from the image analysis. Both pieces of information are independent from the observed spectrum in the NE clump region (the blue spectrum). Yet, the subtracted spectrum (black) of the blue and orange spectra shows almost no absorption lines, indicating strongly that the "pure" spectrum is indeed dominated by the young populations.

To give a quantitative evaluation on how young the "pure" spectrum can be, we compare the obtained "pure" spectrum with a synthesized spectrum of young stellar ages. We construct the spectrum using a software called `Prospector`. `Prospector` (Johnson et al. 2021) accommodates both the single stellar population (SSP) models and the nebular emission models. It can produce a model spectrum with both a continuum and emission lines given a fix set of parameters, such as the age of this spectrum, the dust parameters, and the metallicity of the gas and stars. We list the details of our model as follows.

1. SSP models are from the `FSPS` software (Conroy et al. 2009; Conroy & Gunn 2010), which is connected to `Prospector` by python-fsps (Foreman-Mackey et al. 2014). The stellar spectral library, isochrone model, and stellar initial mass function (IMF) we used are `MILES` (Sánchez-Blázquez et al. 2006), `MIST` (Choi et al. 2016), and the Salpeter IMF (Salpeter 1955), respectively. To model the spectrum of a metal-poor component, we fix the metallicity [Z/H] at −0.4 according to the median value of the metallicity map in the host galaxy region (the right panel of Figure 3).

2. The `CLOUDY` software (Ferland et al. 2013; Byler et al. 2017) is used to model the nebular emission. The metallicity of gas, $[Z/H]_{gas}$, is set to be −0.6 according to the median value of the metallicity map in the NE clump region (the right panel of Figure 3).

3. The dust attenuation model we used (Kriek & Conroy 2013) consists of two components: the dust in the birth cloud around young stars and the diffuse dust in the interstellar medium. The optical depth of the diffuse dust, τ_{diff}, is 0.001. There is a degeneracy between the

stellar population and the dust attenuation—a younger stellar population is expected when using a higher dust attenuation. We use the default value of the optical depth ratio of the birth cloud dust to the diffuse dust, $\tau_{bc}/\tau_{diff} = 1$, and the default value of the diffuse dust index, $n_{diff} = 0$, which regulates the shape of the attenuation curve.

With these parameters set, we use `Prospector` to generate a spectrum with just $\leqslant 7$ Myr stellar population, and show the result in yellow in Figure 8. The model has a continuous constant SFR within the last 0–7 Myr with a total stellar mass of $1.8 \times 10^6\ M_\odot$. The synthesized model spectrum matches very well with the black spectrum. The residual between the model and the "pure" clump spectrum is very small, and we show it in the lower panel in Figure 8. Also shown in the lower panel is the blue shaded region, which is the 3σ region of the observed spectrum of the NE clump (the light blue spectrum). The errors are estimated from the observed flux errors of the spectra of all of the spaxels in the red circle, also considering the covariance of the spaxels (Law et al. 2016). Most of the residuals are within the error bars of the observed spectrum.

The extremely young stellar population required by the good-matching synthesized model seems to suggest that the dominating stellar populations in the "pure" NE clump are very young, and the old stellar populations are quite insignificant. Based on the argument we listed earlier, this may imply that the NE clump is triggered by the gas accretion scenario.

Of course, this analysis can not exclude scenarios of mergers of gas-rich dwarfs that do not have significant old stellar populations compared to the host galaxy of MaNGA 8313-1901 from the beginning. Even though insignificant, we try to give a quantitative constraint on the amount of the old stellar population the "pure" NE clump can have. We notice that within the error bars, the residual spectrum of the "pure" NE clump subtracted by the 7 Myr young stellar population model spectrum does show an offset that seems to grow increasingly larger at longer wavelengths. If this offset is real, it could be accounted for by an old stellar population component. We use the difference of the z-band flux between the model spectrum (estimated to be 1.57×10^{-17} erg s^{-1} cm^{-2}) and the "pure" clump spectrum (estimated to be 1.98×10^{-17} erg s^{-1} cm^{-2}) to estimate the corresponding mass of this possible old stellar population. We choose an SSP template of 10 Gyr old and $[Z/H]_{star} = 0$ to make the estimation; the age of the SSP is chosen to be old enough so that the mass is unlikely to be
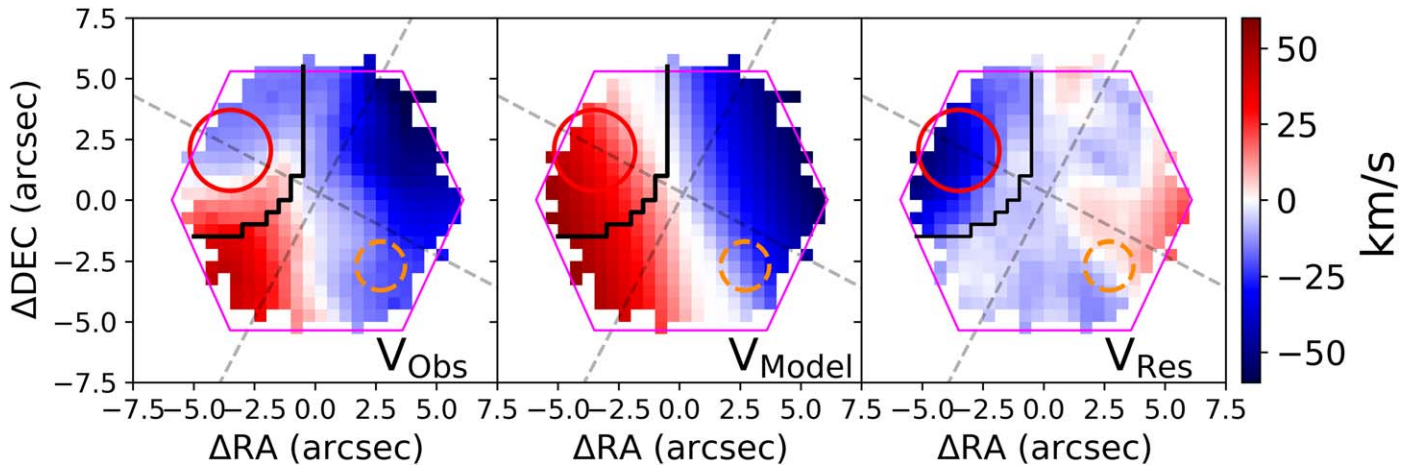
Figure 7. The observed Hα velocity map (the left panel), the best-fit rotation model for the host galaxy (the middle panel), and the residuals ($V_{\rm obs} - V_{\rm model}$) of the Hα velocity field (the right panel) of MaNGA8313-1901.

underestimated. Taking an M/L ratio at the z band of 1.72 ($M_\odot/L_{\odot,z}$) for such a stellar population (Bruzual & Charlot 2003), we estimate the mass of this possible old SSP to be about $3.89 \times 10^7\ M_\odot$. This is only ∼20% of the mass of the underlying host component in the red circle, and ∼1% of the mass of the total host galaxy. Remember that the "pure" clump spectrum (the black spectrum in Figure 8) is obtained via a very simple subtraction method, and there are many uncertainties that can easily account for the ∼20% differences in the flux. Our synthesized model spectrum (the yellow spectrum in Figure 8) is also simple. Thus, we do not make an attempt to interpret these evaluations further. We think it is safe to say that even if the old stellar population exists, it is very insignificant compared to the host galaxy.

The mass of the H I gas of MaNGA 8313-1901 is $\log(M_{\rm HI}/M_\odot) = 9.37$ (Masters et al. 2019). Combining with its stellar mass $\log(M_*/M_\odot) = 8.88$ (also listed in Table 1), the gas-to-stellar mass ratio of MaNGA 8313-1901 is about three, which is quite typical for galaxies with similar stellar masses. This suggests that there is no obvious gas excess in this galaxy. In the gas accretion scenario, since the metallicity of the NE clump is ∼0.1–0.2 dex lower than that of the host galaxy (Figures 5 and 6), we speculate that the accreted gas is metal-poor; otherwise, it should require a significant amount of accreting gas to lower the metallicity of a big index as observed in our case. Assuming that the accreted gas has a metallicity one-tenth of that of the host ($Z_{\rm gas} = Z_{\rm host}/10$), to lower the metallicity in the NE clump region by 0.15 dex, the mass of the accreted gas should be about half of that of the gas already existing in the NE clump region. Considering that there is no obvious gas excess observed in this galaxy, the metallicity of the accreted gas would then be expected to be significantly lower than that of the host, possibly even be the pristine gas.

In addition, the NE clump is located on the major axis of MaNGA 8313-1901. This probably means that the gas is accreted along this direction. Due to the projection effect, we are not certain if the accretion direction is along the disk plane, or have an angle with it. However, it is interesting to see that the SW clump (the orange circle in all of the 2D maps shown in this paper) mentioned in Section 3.2 is also found on the major axis. Even though the metallicity (the middle panel of Figure 3), the EW(Hα) (the bottom-right panel of Figure 1), and the kinematics (Figure 7) of the SW clump are all only

marginally different from its surroundings, we still think that the SW clump is similar to the NE clump and has an external origin, instead of being a part of the disk. A suggestive clue comes from Figure 10, where we show the i-band image from the Hyper Suprime-Cam Subaru Strategic Program on the 8.2 m Subaru Telescope (HSC-SSP; Aihara et al. 2018, 2022). The image is deeper and is of higher spatial resolution compared to the SDSS or the DESI Legacy images. The image shows that there may exist multiple clumps including the NE and the SW clumps, distributed along the major axis of the galaxy, which we tentatively mark with white circles in Figure 10. They may all be part of the same accretion event. Images with even higher spatial resolution are needed to explore this further.

5. Summary

In this paper, we report a BCD galaxy, MaNGA 8313-1901, that has a distinct off-centered clump in the northeast direction, which we name the NE clump. We use GALFIT to obtain the structural information of the host galaxy and the NE clump. We fit the host galaxy and the NE clump with a Sérsic model convolving the PSF. The effective radius and the Sérsic index of the host galaxy are $r_e = 1.23 \pm 0.13$ kpc and $n = 1.46 \pm 0.04$, respectively. Those of the NE clump are $r_e = 290 \pm 12$ pc and $n = 0.19 \pm 0.04$, respectively. The size of the NE clump is significantly larger than typical H II regions seen in local galaxies, and is more similar to the starburst clumps in the high-z galaxies.

We derive the SFR map and the gas-phase metallicity map for this galaxy from the MaNGA data cube. The NE clump shows features of enhanced star formation and lowered metallicity. Different metallicity indicators consistently show that the NE clump has lower metallicity compared to the host. We further study the gas kinematic map as inferred from the Hα emission lines. By building a kinematic model of the Hα velocity map, we find that the NE clump is kinematically detached from the rotating disk of the host galaxy. The lowered metallicity, enhanced star formation, and detached kinematics of the NE clump all imply that the clump did not internally originate as part of the disk, such as an H II complex. Instead, we prefer an external origin for the NE clump. Processes such as the gas accretion or galaxy mergers can all produce large clumps with characters similar to the NE clump. We further
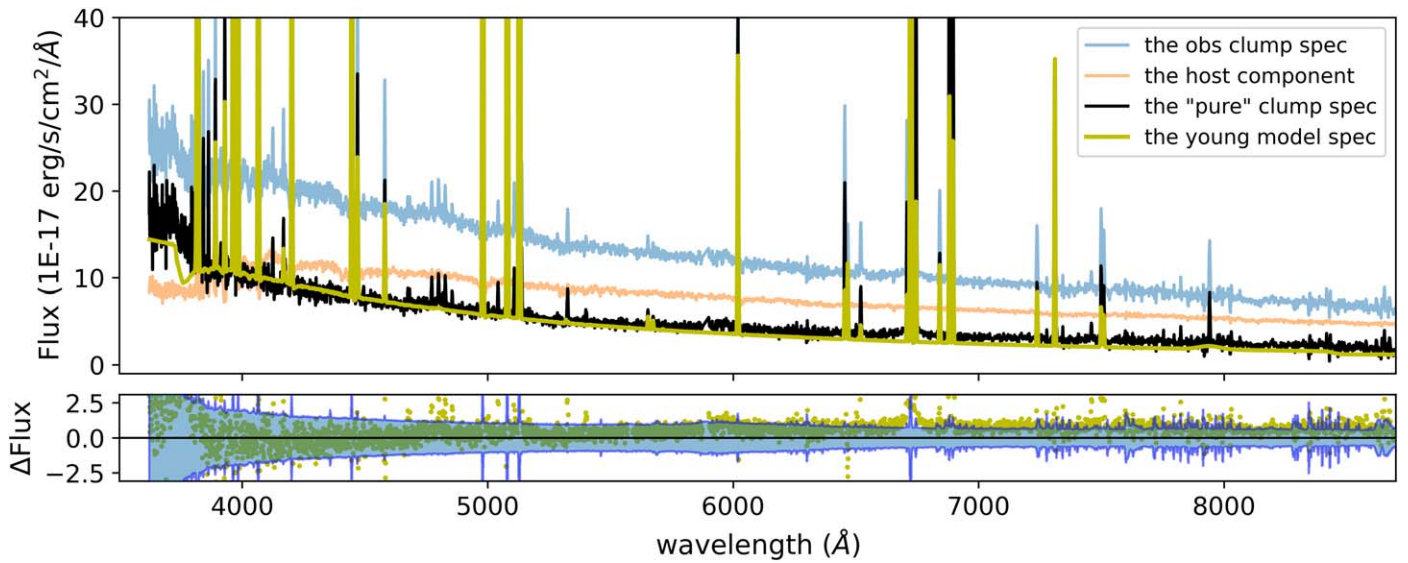
Figure 8. The spectra of different components in the NE clump of MaNGA 8313-1901. In the upper panel, the observed spectrum in the NE clump is shown in light blue. The light orange line represents the estimated host component in the NE clump. The "pure" clump spectrum, i.e., the observed clump spectrum (light blue) subtracted by the estimated host spectrum (light orange), is shown in black. The yellow dashed spectrum shows the modeled clump spectrum constructed by Prospector (see the text for details). The residual of the modeled "pure" clump spectrum, i.e., the difference between the "pure" clump spectrum and the modeled one, is shown in the lower panel. The blue shaded area shows the 3σ error region of the observed spectrum.
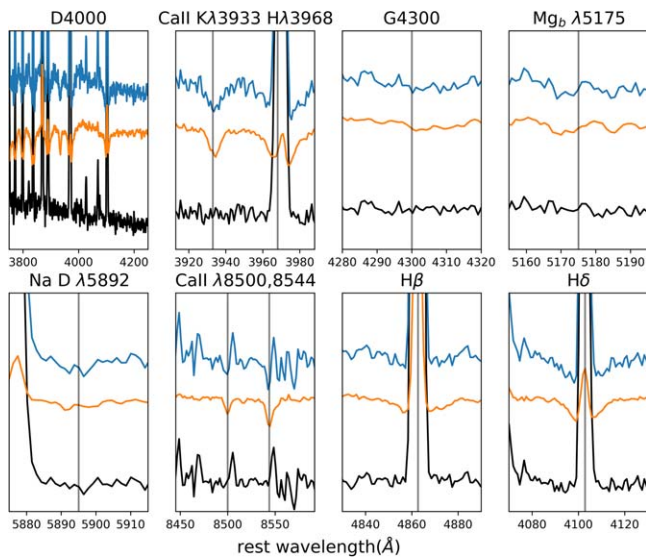
Figure 9. The zoomed-in spectra of the observed spectrum (the blue line), the host-component spectrum (the orange line), and the "pure" clump spectrum (the black line). From top left to bottom right, we show the D4000 absorption lines, Ca II $\lambda3933$, 3968, $G4300$, Mg$_b\lambda5175$, NaD $\lambda5892$, and Ca II $\lambda8500$, 8544, and emission lines Hβ and Hδ.

Figure 10. The i-band image of the HSC survey. We draw four white circles to highlight the small knots that we find.

analyze the stellar populations in the NE clump to explore whether the NE clump contains old stars of its own, aiming to distinguish the scenarios between the gas accretion and the galaxy interaction with significant preexisting old stars.

In order to study the stellar population of the NE clump itself, we need to properly subtract the underlying host component from the observed spectrum of the NE clump region. We assume that the spectral shape of the host component in the NE clump is the same as the center of the host galaxy. We scale the host spectra with the flux of the host component in the NE clump estimated from our best-fit morphological Sérsic model. This spectra of the underlying host component in the NE clump region is shown in Figure 8 as

light orange. The subtraction of the observed clump spectrum (light blue) and the underlying host spectrum (light orange) results in the "pure" clump spectrum (black in Figure 8). It shows obvious characteristics of young stellar populations such as the blue continuum and is almost free of absorption lines.

We use Prospector to construct a spectrum with only young stellar populations ($\leqslant 7\,\mathrm{Myr}$) combined with dust, nebular continuum, and emission lines, which is shown as the yellow spectrum in Figure 8. The modeled spectrum agrees very well with the "pure" clump spectrum (shown as black in Figure 8). This suggests that the "pure" clump spectrum indeed predominantly consists of young stellar populations. The lack of significant old stars in the NE clump favors the gas accretion scenario that the gas in the NE clump may be newly accreted. Of course, we can not exclude scenarios of mergers of gas-rich dwarfs that do not have significant old stellar population

compared to the host galaxy of MaNGA 8313-1901 from the beginning.

In addition to the NE clump, there is another low-metallicity region to the southwest of the host galaxy, which we call the SW clump. The SW clump shows similar characteristics to the NE clump in the SFR, gas-phase metallicity, and kinematics, but to a lesser extent compared with the NE clump. Both of the clumps are located on the major axis of the host galaxy. We speculate that the NE and SW clumps might have similar external origins.

The results of this study can help us to better understand the gas accretion in high-z galaxies. Future moderately deep infrared observations can certainly increase our diagnosing power on the old stellar substrate in the NE clump. Further studies with the H I gas content of the galaxy, such as the observations with the Five-hundred-meter Aperture Spherical Radio Telescope and future resolved H I measurements from the Square Kilometre Array, can be very critical. In addition, the future IFU observation in the optical with the Chinese Space Station Telescope (CSST-IFU), can also help to further dissect the clump. The more detailed investigation of the host properties of MaNGA 8313-1901, combined with more BCDs, can also tell us more about their evolutionary scenarios. In fact, we have compiled a sample of BCDs from the MaNGA survey and found at least two other BCDs that may host off-centered clumps, even though the clumps are not as significant as those shown in MaNGA 8313-1901. We will study them in more detail in the future.

ORCID iDs

Mengting Ju (居梦婷) ⓘ https://orcid.org/0000-0002-5815-2387
Jun Yin (尹君) ⓘ https://orcid.org/0000-0002-4499-1956
Rongrong Liu (刘蓉蓉) ⓘ https://orcid.org/0000-0001-5968-1144
Lei Hao (郝蕾) ⓘ https://orcid.org/0000-0003-2478-9723
Zhengyi Shao (邵正义) ⓘ https://orcid.org/0000-0001-8611-2465
Shuai Feng (冯帅) ⓘ https://orcid.org/0000-0002-9767-9237
Rogério Riffel ⓘ https://orcid.org/0000-0002-1321-1320
Chenxu Liu (刘辰旭) ⓘ https://orcid.org/0000-0001-5561-2010
David V. Stark ⓘ https://orcid.org/0000-0002-3746-2853
Shiyin Shen (沈世银) ⓘ https://orcid.org/0000-0002-3073-5871
José G. Fernández-Trincado ⓘ https://orcid.org/0000-0003-3526-5052
Junfeng Wang (王俊峰) ⓘ https://orcid.org/0000-0003-4874-0369
Haiguang Xu (徐海光) ⓘ https://orcid.org/0000-0001-9405-0137
Dmitry Bizyaev ⓘ https://orcid.org/0000-0002-3601-133X
Yu Rong (容昱) ⓘ https://orcid.org/0000-0002-2204-6558

References

Aihara, H., Arimoto, N., Armstrong, R., et al. 2018, PASJ, 70, S4
Aihara, H., AlSayyad, Y., Ando, M., et al. 2022, PASJ, 74, 247
Allen, J. T., Croom, S. M., Konstantopoulos, I. S., et al. 2015, MNRAS, 446, 1567
Altay, G., Theuns, T., Schaye, J., Booth, C. M., & Dalla Vecchia, C. 2013, MNRAS, 436, 2689

Amorín, R., Aguerri, J. A. L., Muñoz-Tuñón, C., & Cairós, L. M. 2009, A&A, 501, 75

Andersen, D. R., & Bershady, M. A. 2013, ApJ, 768, 41

Baldwin, J. A., Phillips, M. M., & Terlevich, R. 1981, PASP, 93, 5

Belfiore, F., Westfall, K. B., Schaefer, A., et al. 2019, AJ, 158, 160

Blanton, M. R., Bershady, M. A., Abolfathi, B., et al. 2017, AJ, 154, 28

Blum, R. D., Burleigh, K., Dey, A., et al. 2016, AAS Meeting Abstracts, 228, 317.01

Bruzual, G., & Charlot, S. 2003, MNRAS, 344, 1000

Bundy, K., Bershady, M. A., Law, D. R., et al. 2015, ApJ, 798, 7

Byler, N., Dalcanton, J. J., Conroy, C., & Johnson, B. D. 2017, ApJ, 840, 44

Calzetti, D., Armus, L., Bohlin, R. C., et al. 2000, ApJ, 533, 682

Chen, Y.-M., Shi, Y., Tremonti, C. A., et al. 2016, NatCo, 7, 13269

Choi, J., Dotter, A., Conroy, C., et al. 2016, ApJ, 823, 102

Cid Fernandes, R., Mateus, A., Sodré, L., Stasińska, G., & Gomes, J. M. 2005, MNRAS, 358, 363

Cignoni, M., Sacchi, E., Tosi, M., et al. 2019, ApJ, 887, 112

Conroy, C., & Gunn, J. E. 2010, ApJ, 712, 833

Conroy, C., Gunn, J. E., & White, M. 2009, ApJ, 699, 486

Crain, R. A., Theuns, T., Dalla Vecchia, C., et al. 2009, MNRAS, 399, 1773

Cresci, G., Mannucci, F., Maiolino, R., et al. 2010, Natur, 467, 811

Croom, S. M., Lawrence, J. S., Bland-Hawthorn, J., et al. 2012, MNRAS, 421, 872

Dekel, A., Birnboim, Y., Engel, G., et al. 2009, Natur, 457, 451

Denicoló, G., Terlevich, R., & Terlevich, E. 2002, MNRAS, 330, 69

Dey, A., Schlegel, D. J., Lang, D., et al. 2019, AJ, 157, 168

Drory, N., MacDonald, N., Bershady, M. A., et al. 2015, AJ, 149, 77

Elmegreen, B. G., Elmegreen, D. M., Sánchez Almeida, J., et al. 2013, ApJ, 774, 86

Ferland, G. J., Porter, R. L., van Hoof, P. A. M., et al. 2013, RMxAA, 49, 137

Finlator, K., & Davé, R. 2008, MNRAS, 385, 2181

Fitzpatrick, E. L. 1999, PASP, 111, 63

Foreman-Mackey, D., Hogg, D. W., Lang, D., & Goodman, J. 2013, PASP, 125, 306

Foreman-Mackey, D., Sick, J., & Johnson, B. 2014, python-fsps: Python bindings to FSPS v0.1.1, Zenodo, doi:10.5281/zenodo.12157

Fraternali, F. 2014, IAUS, 298, 228

Fumagalli, M., Prochaska, J. X., Kasen, D., et al. 2011, MNRAS, 418, 1796

Ge, J., Mao, S., Lu, Y., et al. 2021, MNRAS, 507, 2488

Genel, S., Dekel, A., & Cacciato, M. 2012, MNRAS, 425, 788

Gunn, J. E., Siegmund, W. A., Mannery, E. J., et al. 2006, AJ, 131, 2332

Guseva, N. G., Izotov, Y. I., Papaderos, P., & Fricke, K. J. 2007, A&A, 464, 885

Hao, C.-N., Kennicutt, R. C., Johnson, B. D., et al. 2011, ApJ, 741, 124

Henry, A., Martin, C. L., Finlator, K., & Dressler, A. 2013, ApJ, 769, 148

Hernandez, A. K., Wakker, B. P., Benjamin, R. A., et al. 2013, ApJ, 777, 19

Hwang, H.-C., Barrera-Ballesteros, J. K., Heckman, T. M., et al. 2019, ApJ, 872, 144

Ji, X., Li, C., Yan, R., et al. 2021, MNRAS, 508, 3943

Jin, Y., Chen, Y., Shi, Y., et al. 2016, MNRAS, 463, 913

Johnson, B. D., Leja, J., Conroy, C., & Speagle, J. S. 2021, ApJS, 254, 22

Joung, M. R., Bryan, G. L., & Putman, M. E. 2012, ApJ, 745, 148

Kang, X., Chang, R., Yin, J., et al. 2012, MNRAS, 426, 1455

Kauffmann, G., Heckman, T. M., White, S. D. M., et al. 2003a, MNRAS, 341, 33

Kauffmann, G., Heckman, T. M., Tremonti, C., et al. 2003b, MNRAS, 346, 1055

Kennicutt, R. C. J. 1998, ApJ, 498, 541

Kennicutt, R. C., & Evans, N. J. 2012, ARA&A, 50, 531

Kewley, L. J., Dopita, M. A., Sutherland, R. S., Heisler, C. A., & Trevena, J. 2001, ApJ, 556, 121

Kriek, M., & Conroy, C. 2013, ApJL, 775, L16

Lagos, P., Telles, E., & Melnick, J. 2007, A&A, 476, 89

Lagos, P., Telles, E., Nigoche-Netro, A., & Carrasco, E. R. 2011, AJ, 142, 162

Lassen, A. E., Riffel, R., Chies-Santos, A. L., et al. 2021, MNRAS, 506, 3527

Law, D. R., Yan, R., Bershady, M. A., et al. 2015, AJ, 150, 19

Law, D. R., Cherinka, B., Yan, R., et al. 2016, AJ, 152, 83

Law, D. R., Westfall, K. B., Bershady, M. A., et al. 2021, AJ, 161, 52

Lima-Costa, F., Martins, L. P., Rodríguez-Ardila, A., & Fraga, L. 2020, A&A, 642, A203

Lin, L., Lin, J.-H., Hsu, C.-H., et al. 2017, ApJ, 837, 32

Liu, C., Hao, L., Wang, H., & Yang, X. 2019, ApJ, 878, 69

Mallmann, N. D., Riffel, R., Storchi-Bergmann, T., et al. 2018, MNRAS, 478, 5491

Mannucci, F., Cresci, G., Maiolino, R., Marconi, A., & Gnerucci, A. 2010, MNRAS, 408, 2115

Marino, R. A., Rosales-Ortega, F. F., Sánchez, S. F., et al. 2013, A&A, 559, A114

Masters, K. L., Stark, D. V., Pace, Z. J., et al. 2019, MNRAS, 488, 3396

Meng, X., & Gnedin, O. Y. 2020, MNRAS, 494, 1263

Pace, Z. J., Tremonti, C., Schaefer, A. L., et al. 2021, ApJ, 908, 165

Pagel, B. E. J., Edmunds, M. G., Blackwell, D. E., Chun, M. S., & Smith, G. 1979, MNRAS, 189, 95

Pan, H.-A., Lin, L., Hsieh, B.-C., et al. 2020, ApJ, 903, 16

Papaderos, P., & Östlin, G. 2012, A&A, 537, A126

Peng, C. Y., Ho, L. C., Impey, C. D., & Rix, H.-W. 2002, AJ, 124, 266

Peng, C. Y., Ho, L. C., Impey, C. D., & Rix, H.-W. 2010, AJ, 139, 2097

Peng, Y.-j., & Maiolino, R. 2014, MNRAS, 443, 3643

Pérez-Montero, E. 2014, MNRAS, 441, 2663

Pettini, M., & Pagel, B. E. J. 2004, MNRAS, 348, L59

Rauch, M., Becker, G. D., Haehnelt, M. G., et al. 2011, MNRAS, 418, 1115

Richards, S. N., Schaefer, A. L., López-Sánchez, Á R., et al. 2014, MNRAS, 445, 1104

Riffel, R., Mallmann, N. D., Ilha, G. S., et al. 2021, MNRAS, 501, 4064

Salpeter, E. E. 1955, ApJ, 121, 161

Sánchez, S. F., Pérez, E., Sánchez-Blázquez, P., et al. 2016a, RMxAA, 52, 21

Sánchez, S. F., Pérez, E., Sánchez-Blázquez, P., et al. 2016b, RMxAA, 52, 171

Sánchez Almeida, J., Elmegreen, B. G., Muñoz-Tuñón, C., & Elmegreen, D. M. 2014, A&ARv, 22, 71

Sánchez Almeida, J., Elmegreen, B. G., Muñoz-Tuñón, C., et al. 2015, ApJL, 810, L15

Sánchez-Blázquez, P., Peletier, R. F., Jiménez-Vicente, J., et al. 2006, MNRAS, 371, 703

Silva, D. R., Blum, R. D., Allen, L., et al. 2016, AAS Meeting, 228, 317.02

Smee, S. A., Gunn, J. E., Uomoto, A., et al. 2013, AJ, 146, 32

Stewart, K. R., Kaufmann, T., Bullock, J. S., et al. 2011, ApJ, 738, 39

Storchi-Bergmann, T., Calzetti, D., & Kinney, A. L. 1994, ApJ, 429, 572

Telles, E., & Melnick, J. 2018, A&A, 615, A55

Thilker, D. A., Bianchi, L., Meurer, G., et al. 2007, ApJS, 173, 538

Tremonti, C. A., Heckman, T. M., Kauffmann, G., et al. 2004, ApJ, 613, 898

Wake, D. A., Bundy, K., Diamond-Stanic, A. M., et al. 2017, AJ, 154, 86

Wang, H., Mo, H. J., Yang, X., et al. 2016, ApJ, 831, 164

Wang, H., Mo, H. J., Chen, S., et al. 2018, ApJ, 852, 31

Westfall, K. B., Cappellari, M., Bershady, M. A., et al. 2019, AJ, 158, 231

Willett, K. W., Lintott, C. J., Bamford, S. P., et al. 2013, MNRAS, 435, 2835

Williams, G. G., Olszewski, E., Lesser, M. P., & Burge, J. H. 2004, Proc. SPIE, 5492, 787

Wuyts, E., Rigby, J. R., Gladders, M. D., & Sharon, K. 2014, ApJ, 781, 61

Yan, R., Bundy, K., Law, D. R., et al. 2016a, AJ, 152, 197

Yan, R., Tremonti, C., Bershady, M. A., et al. 2016b, AJ, 151, 8

Yang, X., Mo, H. J., van den Bosch, F. C., et al. 2007, ApJ, 671, 153

Yang, X., Mo, H. J., van den Bosch, F. C., Zhang, Y., & Han, J. 2012, ApJ, 752, 41

Yates, R. M., Kauffmann, G., & Guo, Q. 2012, MNRAS, 422, 215

Yin, J., Hou, J. L., Prantzos, N., et al. 2009, A&A, 505, 497

Zou, H., Zhou, X., Fan, X., et al. 2017, PASP, 129, 064101